scientific reports

OPEN

Superior visible light antimicrobial performance of facet engineered cobalt doped TiO$_2$ mesocrystals in pathogenic bacterium and fungi

Ayat N. El-Shazly[1,2,6], Gharieb S. El-Sayyad[3,6], Aiat H. Hegazy[4,6], Mahmoud A. Hamza[5], Rasha M. Fathy[3], E. T. El Shenawy[4] & Nageh K. Allam[1]✉

Pristine and Co-doped TiO$_2$ mesocrystals have been synthesized via a simple sol–gel method and their antimicrobial activity has been investigated. The antimicrobial performance was evaluated in terms of zone of inhibition, minimum inhibitory concentration (MIC), antibiofilm activity, and effect of UV illumination in liquid media. The Co-doped TiO$_2$ mesocrystals showed very promising MIC of 0.390 μg/mL and 0.781 μg/mL for *P. mirabilis* and *P. mirabilis*, respectively. Additionally, the material showed an MIC of 12.5 μg/mL against *C. albicans*, suggesting its use as antifungal agent. Upon the addition of 10.0 μg/mL of Co-doped TiO$_2$ mesocrystals, the biofilm inhibition% reaches 84.43% for *P. aeruginosa*, 78.58% for *P. mirabilis*, and 77.81% for *S. typhi*, which can be ascribed to the created active oxygen species that decompose the tested microbial cells upon illumination. Thus the fabricated Co-doped TiO$_2$ mesocrystals exhibit sufficient antimicrobial features under visible light, qualifying them for use as antimicrobial agents against pathogenic bacteria and fungi and subsequently inhibit their hazardous effects.

In the last decades, a lot of efforts have been devoted towards the synthesis of nanomaterials with unique physical, chemical, and biological characteristics compared to their bulk counterparts[1,2]. Cölfen et al. first introduced a new class of materials known as mesocrystal[3]. Mesocrystals were proposed to form upon the addition of highly oriented small particles, thus the resulting larger crystals would have single-crystal orientation[4]. Their positive effects in improving charge carriers separation made them good candidates for many applications, such as photocatalysis[5], sensing, and energy storage and conversion[6]. For instance, TiO$_2$ mesocrystals become a research hotspot for biomedical and food applications due to their antimicrobial characteristics[7]. Besides, their chemical stability, abundance, low cost, eco-friendly made them good candidates for photovoltaics[8], hydrogen production[9] and wastewater treatment[10]. Upon irradiated by UV light, the anatase phase of TiO$_2$ can oxidize and reduce oxygen and water to produce reactive oxygen species (ROS), such as superoxide radicals and hydroxyl radicals[11]. These ROS play a key role in destroying pathogenic bacteria and fungi by damaging their critical molecular components[12,13]. However, the practical application of TiO$_2$ photocatalysts is limited by their wide bandgap energy (3.0–3.2 eV), limited to the UV region of the light spectrum with low efficiency of solar light energy utilization[14–18]. To enhance the photocatalytic response of TiO$_2$, many strategies have been implemented, such as metal and nonmetal doping, annealing in reducing atmosphere, creating defects in the crystal lattice, and coupling with various light harvesters[16,19,20]. Doping TiO$_2$ with transition metals, such as Fe, Ni, Cr, and Co, was shown to enhance its photoactivity by creating shallow states that suppress the e–h pairs recombination[21,22]. Moreover, multi-doping with two or three metal or non-metal elements, such as N, C, and Ce or Co, Cu, Ir, C, and Ti^{3+}, was shown to improve the conductivity and balance the deficiencies of individual dopants[23,24]. Consequently, multi-doped TiO$_2$ has gained much attention compared to the singly and doubly-doped counterparts. The origin of the super reactivity of multi-doped TiO$_2$ seems to be the synergistic effect of the dopants in narrowing the

[1]Energy Materials Laboratory, School of Sciences and Engineering, The American University in Cairo, New Cairo 11835, Egypt. [2]Central Metallurgical Research and Development Institute, Helwan, P.O. Box 87, Cairo, Egypt. [3]Drug Microbiology Lab., Drug Radiation Research Department, National Center for Radiation Research and Technology (NCRRT), Egyptian Atomic Energy Authority (EAEA), Cairo, Egypt. [4]Solar Energy Department, National Research Centre, Giza, Dokki, Egypt. [5]Chemistry Department, Faculty of Science, Ain Shams University, Abbassia, Cairo, Egypt. [6]These authors contributed equally: Ayat N. El-Shazly, Gharieb S. El-Sayyad and Aiat H. Hegazy. ✉email: nageh.allam@aucegypt.edu

bandgap, enhancing the concentration of reactive radical species[25], and enhancing visible light absorption[24]. In this regard, identifying a one-step synthesis method of multi-doped TiO_2 is extremely desirable, which remains a challenge to be realized. Herein, we report on the successful fabrication of cobalt, Ti^{3+}, and carbon multi-doped TiO_2 mesocrystals via an in-situ sol–gel process. The antimicrobial behavior of the fabricated mesocrystals was investigated at ambient conditions and under light illumination. Finally, the reaction mechanism of TiO_2 and multi-doped TiO_2 mesocrystals-treated microbial cells was suggested and discussed in details. Thus, the innovative points of this research include the one-pot synthesis with controlled amount of dopants, the defective structures and how defects played a role in the antibacterial properties as well as the superior dual bacterial and fungi inhibition functions.

Materials and methods

Titanium n-propoxide (Ti(O-n-Pr)$_4$, 98%), cobalt nitrate hexahydrate (Co (NO$_3$)$_2$·6H$_2$O), Formamide (FA: H$_2$N-CHO), and hydrofluoric acid (HF 40%) were purchased from Sigma-Aldrich. Microbiological media ingredients were purchased from Oxford, and reagents used in the biological tests were obtained from Sigma-Aldrich. All the other chemicals were of pure grade and used as received without any further purification. All the solutions were prepared using distilled water (DW).

Synthesis of TiO$_2$ mesocrystals. The proposed TiO$_2$ mesocrystals were fabricated using a facile one-pot synthesis method, inspired by the work reported by Hegazy and Prouzet[26]. Typically, 3 mL of HF was added dropwise to 4.84 mL of Ti(O-n-Pr)$_4$ with vigorous stirring in an ice bath. Then, 5.2 mL of a solution of FA in DW (86%, v/v) were added dropwise to the previous solution, which was left for 2 h at room temperature. The resulting gel was dried at 100 °C for 4 h and calcined in air at 400 °C for 4 h[18]. The Co-doped TiO$_2$ mesocrystals were synthesized according to the same procedure by dissolving 0.5 g (Co(NO$_3$)$_2$) in the mixture of FA/DW.

Physicochemical characterizations and antimicrobial activities of TiO$_2$ and Co-doped TiO$_2$ mesocrystals. The crystal properties of the as-synthesized samples were investigated by X-ray diffraction (XRD) patterns recorded on PANalytical X'Pert PRO X-ray diffractometer with Cu Kα radiation (λ = 0.15418 nm, 2θ range = 5°:80°, step size = 0.04°, and scan-step time = 0.5 s). Raman measurements were performed on a Raman microscope (Pro Raman-L Analyzer) with an excitation laser beam wavelength of 532 nm. Fourier transform infrared (FTIR) spectra were recorded on Nicolet 380 Thermo-Scientific in the range of 400–4000 cm^{-1}. The elemental composition was assessed using Thermo-Scientific ESCALAB 250Xi X-ray photoelectron spectroscopy (XPS). The morphological analysis of the as-synthesized nanoparticles was performed using a Zeiss SEM Ultra 60 field-emission scanning electron microscope (FESEM) operating at an accelerating voltage of 5 kV. The nanostructure of the samples was investigated using JOEL JEM-2100 high-resolution transmission electron microscope (HR-TEM) operating at an accelerating voltage of 200 kV; the sample was prepared by dispersing the TiO$_2$ powder in ethanol followed by dropping a small amount on a standard copper TEM grid containing lacy carbon. The UV–Vis absorption spectra of samples were collected using a Shimadzu UV-2600 UV–Vis–NIR spectrophotometer. The photoluminescence spectra (PL) were recorded using Thermo- Scientific LUMINA fluorescence spectrometer.

The antimicrobial potential of as-synthesized TiO$_2$ mesocrystals, Co-doped TiO$_2$ mesocrystals, and Co^{2+} ions against different pathogenic microbes (yeast and bacteria) are examined via employing the agar-disc diffusion method[12]. Firstly, the as-synthesized TiO$_2$ mesocrystals, and Co^{2+} ions are dissolved into distilled water with concentrations 0.01 mg/mL; 10 ppm. The activity of the as-synthesized compounds are examined against different types of bacteria, namely *Staphylococcus aureus*, *Pseudomonas aeruginosa*, *Escherichia coli*, *Klebsiella pneumoniae*, Methicillin-resistant *Staphylococcus aureus* (MRSA), *Proteus vulgaris*, *Salmonella typhi*, and *Proteus mirabilis*. The examined multi-drug resistance bacteria were tested by Vitek two systems (bioMarieux and Marcy-LEtoile, France). Most of them were resistant to antibiotics like Cefapirin, Ciprofloxacin, Amikacin, Norfloxacin, Amoxicillin, Cefoxitin, Gentamicin, Ampicillin, and Cefotaxime. In the microbiological experiments, we performed the biosafety Level-2 (BSL-2). It should be noted that all the inoculums are established and fixed from 2–5 × 10^8 CFU/mL (0.5 McFarland; at 600 nm). The inhibition of the bacterial growth was defined by the zone of inhibition (ZOI) after 24 h of incubation. Additionally, the antifungal potential of the as-synthesized TiO$_2$ mesocrystals, and Co^{2+} ions is examined against pathogenic unicellular fungi (*Candida albicans* and *Candida tropicalic*). After that, the inoculums of the tested yeast cells are set from 1–4 × 10^7 CFU/mL. Finally, Nystatin (NS) and Amoxicillin (AX) are conducted as standard antibiotics. AX is similar to penicillin in its bactericidal action against susceptible bacteria during the stage of active multiplication. It acts via the inhibition of cell wall biosynthesis that leads to the death of the bacteria. While, NS is an antifungal that is both fungi-static and fungicidal in vitro against a wide-variety of yeasts and yeast-like fungi. It exerts its antifungal effects via disruption of the fungal cell membrane.

The minimum inhibitory concentrations (MIC) investigation is completed in Luria–Bertani (LB) broth within a serial dilution. Briefly, a positive control (the microorganism and the nutrient), a negative control (the nutrient solely), and the examined TiO$_2$ mesocrystals (beginning with 0.1 mg/mL concentration; 100 ppm) are applied; MIC is defined following 24 h at 37 °C. The inoculums of the tested bacteria are at 3–5 × 10^8 CFU/mL and 2–3 × 10^7 CFU/mL to *Candida* species. MIC is defined by operating ELISA plate (at 600 nm). Finally, the results are statistically analyzed by applying ONE WAY ANOVA, the least significant difference (LSD), and Duncan's multiple ranges, which are calculated by special software (SPSS version 15).

Antibiofilm activities of Co-doped TiO$_2$ mesocrystals. Moreover, a qualitative measurement regarding the biofilm inhibition was defined as stated by G. Christensen et al.[27]. The noticeable examination of the

biofilm which was performed at the tube wall in the absence and presence of the synthesized TiO_2 mesocrystals was established. The antibiofilm of the as-synthesized TiO_2 mesocrystals (at 10.0 μg/mL) was examined toward the selected bacteria and *Candida* spp., and was determined and compared with the control (non-treated one). Briefly, 5 mL of the nutrient broth medium was added inside all tubes, and the examined bacteria and yeast were inoculated after adjusted 0.5 McFarland to be $1–2.5×10^8$ CFU/mL. After that, they were incubated at $37.0±0.5$ °C for 24 h. The contents presented in control and treated tubes were discarded, mixed with Phosphate Buffer Saline (PBS; pH 7.0), and finally desiccated. Then, the bacterial and yeast cells which adhered to the tube walls were fixed with 5 mL sodium acetate (3.0%) for about 15 min, and finally, they were rinsed with de-ionized water. Biofilms which introduced inside tubes were stained with 15 mL Crystal Violet (CV; 0.1%) and washed with de-ionized water to remove the rest of the CV. It must be noted that, for the semi-quantitative antibiofilm estimation, 5 mL of the absolute ethanol was inserted to dissolve the stained bacterial and yeast biofilms[28–30]. The O.D. of the stained bacterial and yeast biofilms with CV was examined by UV–Vis. spectrophotometer at 570.0 nm. The bacterial and yeast biofilms inhibition percentage was estimated by applying the following relation (Eq. 1)[31]:

$$\text{Biofilm inhibition \%} = \left(\text{O.D.}_{\text{Control sample}} - \text{O.D.}_{\text{treated sample}}\right)/\text{O.D.}_{\text{Control sample}} \times 100. \tag{1}$$

Effect of UV-irradiation on the antimicrobial abilities of the prepared TiO_2 mesocrystals, and Co-doped TiO_2 mesocrystals. Furthermore, the antibacterial activity of the as-synthesized TiO_2 nanoparticles with and without UV illumination was assessed against the tested pathogenic microbes *Pseudomonas aeruginosa*, *Staphylococcus aureus*, and *Candida albicans* strains using the optical density method[32]. The tested microorganisms were stimulated in nutrient broth (NB) overnight at 37 °C. Firstly, 0.5 mL of the overnight culture were inoculated to 5 mL NB tubes that adjusted after 2 h of incubation to standard 0.5 McFarland concentration that standardly equals $1.5×10^8$ CFU of bacteria and 0.400 equal ($1×10^4$ cells/mL) of C. *albicans*. 100 μL of Co-doped TiO_2 mesocrystals were added into the tubes and then incubated at 37 °C for 60 min. While tubes without Co-doped TiO_2 mesocrystals were inoculated with bacteria and used as the positive control (subject to UV), tubes without UV illumination were used as the negative control. Typically, 10-W low-pressure mercury lamp was horizontally-placed on the laminar flow and employed as the UV-irradiation source, where 90% of the emitted irradiation was at the specific wavelength (600 nm for bacteria and 630 nm for the fungi). Finally, test tubes were subject to UV-irradiation for 1 h at a distance of about 61 cm. After the incubation, the turbidity of the medium was measured at λ of 600 nm for bacteria and 630 nm for the fungi.

Reaction mechanism using SEM/EDX analysis of TiO_2 mesocrystals, and Co-doped TiO_2 mesocrystals-treated microbial cells. The sensitive bacterial cells (from the antibiofilm results) were cleaned with Physiological Buffer Saline (PBS) three-times and finally, fixed by 3.5% glutaraldehyde solution. The maintained microbial units were repeatedly-rinsed by PBS and regularly-dried with different concentrations of ethyl alcohol like 30, 50, 70, 90, and 100% for 15 min at $27±2$ °C. Following that, the prepared samples were fixed on an aluminum piece regarding SEM/EDX analysis. The morphological features of the control (non-treated *P. aeruginosa*), TiO_2 mesocrystals, and Co-doped TiO_2 mesocrystals-treated *P. aeruginosa* were examined by SEM/EDX investigation.

Results and discussion
Physicochemical characterization. Figure 1a depicts the XRD patterns of both bare and Co-doped TiO_2 mesocrystals calcinated at 400 °C. Both samples have tetragonal anatase phase with a space group I41/amd (Ref card No.: 04-014-5762). No diffraction peaks for cobalt or cobalt oxide were detected in the Co-doped TiO_2 sample, which may be related to the low cobalt content[33]. However, the main (1 0 1) diffraction peak is shifted to lower 2θ (inset in Fig. 1a), indicating the incorporation of foreign species into the TiO_2 lattice, thus changing the Ti^{4+} local structure[34]. Besides, it was found that there is a low intensity peak at 26.7° in the diffraction pattern of the bare TiO_2 sample, which can be attributed to the main plane (110) of the rutile phase. The intensity of this peak was enhanced after the insertion of cobalt ions as observed in the diffraction pattern of the Co-doped TiO_2 sample. The percentage of both anatase and rutile phases was calculated using Eqs. (2) and (3)[20]:

$$A\% = [0.79\,I_A/\,(I_R + 0.79I_A)] \times 100, \tag{2}$$

$$R\% = [\,I_R/\,(I_R + 0.79I_A)] \times 100, \tag{3}$$

where I_A and I_R are the intensities of XRD peaks of anatase and rutile at 25.3° and 26.7° peaks, respectively. It was found that bare TiO_2 sample is composed of 99% anatase and only 1% rutile, while the Co-doped TiO_2 sample is composed of 93.3% anatase and 6.7% rutile. The increase of rutile% reveals that Co can act as a rutile stabilizer[35]. Although it is generally accepted for pure phases that anatase exhibits a higher photocatalytic activity compared to rutile TiO_2, the existence of very small percent of the rutile phase causes an enhancement in the photocatalytic activity of the samples, even in the case of bare TiO_2 mesocrystals, due to the synergistic effects between the two phases compared to pure phases[19].

The mean crystallite sizes of bare TiO_2 and Co-doped TiO_2 were estimated to be 69 and 40 nm, respectively as determined using Debey–Scherrer formula (Eq. 4), with L being the mean crystallite size (nm), *k* the Scherrer constant related to the crystallite shape (k = 0.9), λ the X-ray wavelength in nanometer (nm), β the full width at half-maximum of the peak in radians, and θ the diffraction angle.
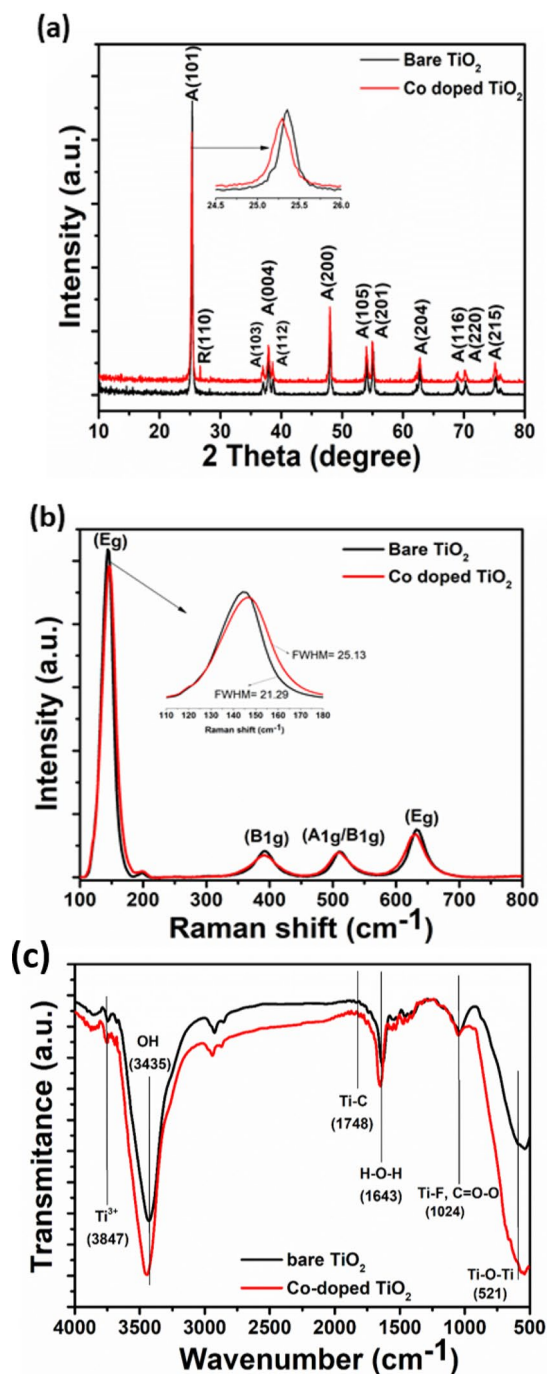
Figure 1. The (**a**) XRD patterns, (**b**) Raman, and (**c**) FT-IR spectra of the bare and Co-doped TiO$_2$ mesocrystals.

$$L = \frac{k\lambda}{\beta \cos\theta}.$$ (4)

Note the decrease in crystallinity upon Co doping, which can be ascribed to the difference between the ionic charge of Ti (+4) and Co (+2). Moreover, Co doping is expected to cause a slight change in the lattice constants. The lattice parameters (*a* and *c*) and cell volume (*V*) were estimated based on Bragg's law and a formula for a tetragonal system (Eq. 5) for both bare TiO$_2$ and Co-doped TiO$_2$ samples.

$$\frac{1}{d^2} = \frac{h^2 + k^2}{a^2} + \frac{l^2}{c^2}.$$ (5)

It was observed that the unit cell volume has been enlarged from 135.66 to 136.612, and the lattice constant "a" from 3.78 to 3.794 for bare TiO_2 and Co-doped TiO_2, respectively. These results may indicate the successful incorporation of Co^{2+} into the anatase TiO_2 lattice.

Raman spectroscopy is an effective tool to elucidate the structural changes in materials upon doping. Based on group theory, anatase TiO_2 exhibits six Raman-active vibrational modes ($3 E_g + 2B_{1g} + A_{1g}$), as displayed in Fig. 1b. The six allowed modes of anatase single crystal were reported by Oshaka[36], where the bands E_{g1} (at 144 cm^{-1}), E_{g2} (at 196 cm^{-1}), and E_{g3} (at 632 cm^{-1}), for Eg modes are related to the O–Ti–O symmetric stretching vibration. The two B_{1g} modes: B_{1g1} at 392 and B_{1g2} at 511 cm^{-1} are related to the O–Ti–O symmetric bending vibration, and the one A1g mode at 512 cm^{-1} is related to the O–Ti–O anti-symmetric bending vibration[37,38]. In the case of Co-doped TiO_2 sample, it is found that the main peaks E_{g1} and E_{g2}, located at 144 cm^{-1} and 196 cm^{-1}, are shifted to higher wavenumbers (147.2 and 199.2 cm^{-1}). However, the E_{g3} peak (632 cm^{-1}) is shifted to a lower wavenumber (629.8 cm^{-1}) compared to that of bare TiO_2. Besides, the B_{1g} and A_{1g} peaks are shifted to 389.6 and 509.7 cm^{-1}, respectively. Furthermore, no bands appeared related to any cobalt oxide phase, probably due to the low Co content in TiO_2 lattice[39]. As the ionic radius of Co^{2+} (0.70 Å) is larger than that of Ti^{4+} (0.64 Å), the insertion of Co as a dopant should lead to a structural distortion and induce oxygen vacancies, which can be the main reason of the observed peak shift. Moreover, electron–phonon coupling is one of the physical parameters used to understand the electron transport and the existence of oxygen vacancies in the lattice of metal oxides[20]. The electron–phonon coupling is related to the phonon linewidth (FWHM) and can be estimated from the energy-time uncertainty relation (Eq. 6)[40]:

$$1/\tau = 2\pi cr, \tag{6}$$

where τ is the phonon lifetime, c is the speed of light (3×10^8 m/s), and r is the FWHM of the Raman peak in units of cm^{-1}. The estimated phonon lifetime is found to decrease from 2.49 to 2.11 ps upon cobalt doping.

The FT-IR spectra of the bare and Co-doped TiO_2 mesocrystals are shown in Fig. 1c. The broad peaks located at 3847, 3837, and 3800 cm^{-1} are ascribed to Ti^{3+}[41]. Besides, the broad peaks at 3435 and 3750 cm^{-1} are likely due to stretching vibrations of adsorbed O–H groups, while the peak at 1748 cm^{-1} arises from Ti–O–C vibration, confirming the effective interaction between Ti and C. The peak at 1643 cm^{-1} is from the H–O–H bending mode[42]. The peak located at 1427 cm^{-1} is assigned to the Ti–O vibrations on the {001} facets[43], in good agreement with the XRD results. Also, the peak at 1024 cm^{-1} is due to Ti–F vibrations in both samples. Moreover, the Ti–O stretching and Ti–O–Ti bridging have appeared between 521 and 460 cm^{-1}. Thus, the FT-IR spectra reveals the presence of Ti^{3+} in the prepared TiO_2 mesocrystals.

In order to investigate the bonding states of the elements on the surface of bare and Co- doped TiO_2, XPS analysis was carried and the data are presented in Fig. 2. The full-scan XPS survey of both samples (Fig. 2a) revealed peaks that are exclusively related to Ti, O, and C, elements in addition to an extra peak of Co in the Co-doped TiO_2 sample. Figure 2b shows the high-resolution XPS spectra of Ti 2p, where Ti 2p$_{3/2}$ and Ti 2p$_{3/2}$ peaks are observed at 459.1 eV and 464.7 eV, respectively for the bare TiO_2 sample. The O1s HR-XPS spectrum (Fig. 2c) is fitted into two-sub peaks centered at 530.26 eV and 532.17 eV for bare TiO_2, and 529.78 and 531.4 eV for Co-doped TiO_2. The peaks at 530.26 eV and 529.78 eV are related to Ti–O and surface OH$^-$ groups[44]. Additionally, the other oxygen peak (530.3 eV) in Co-doped TiO_2 is originated from the presence of Co–O bond[45]. Moreover, the C 1 s peak (Fig. 2d) can be de-convoluted into three peaks in both samples, one located at 284.69 eV and 284.54 eV and others at 285.82 eV, 286.39 eV, 288.67 eV and 288.42 eV for bare and Co-doped TiO_2, respectively. The main peak corresponds to C–C bond that exists in carbon species and the others at higher energy could arise from C–O and C=O bond in TiO_2, revealing interstitial and/or substitutional C[46]. Finally, the Co 2p peaks appeared at 781.8 and 796.42 eV (Fig. 2e) correspond to Co^{2+} 2p$_{3/2}$ and Co^{2+} 2p$_{1/2}$, respectively. Notably, all elements binding energies (Ti, O, and C) in Co-doped TiO_2 sample exhibited a slight negative shift when compared to the bare TiO_2 sample, which can be related to the doping of cobalt ions in TiO_2 lattice where the Co has a higher electronegativity than Ti[47].

Figure 3a,b shows the representative FESEM images of the prepared undoped and cobalt-doped TiO_2 mesocrystals, respectively, revealing agglomerates of highly connected of small particles with homogenous size distribution. Upon Co-doping, a notable decrease in the size of the particles was observed, revealing the effect of cobalt insertion on retarding the TiO_2 growth[48]. The EDX analysis (insets in Fig. 3e,f) reveals the presence of Ti, O, C, and Co without any impurities. Figure 3c–f depicts typical HR-TEM images of the TiO_2 mesocrystals before and after doping with cobalt, viewed along a square surface of {001} crystallographic direction. Note also the presence of a carbon shell as indicated by an arrow in Fig. 3e,f. The transparent carbon layer is uniform and continuously surrounding the TiO_2 mesocrystals[49,50]. Raman spectroscopy was used to confirm the presence of the residual carbon (insets in Fig. 3e,f), where the peaks at 1400 and 1290 cm^{-1} are mainly originating from sp^3 hybridization (D-band) and the planar configuration of the sp^2-bonded carbon structure (G-band), respectively[51].

The optical absorption of the bare and Co-doped TiO_2 mesocrystals was elucidated by recording their UV–Vis diffuse reflectance spectra (DRS) as shown in Supplementary Fig. S1a. Both samples exhibit visible light response in the wavelength range of 400–600 nm. The spectra of bare TiO_2 sample (Supplementary Fig. S1a) reveal an absorption edge at 418 nm, which is redshifted relative to that reported for P25 (TiO_2)[52]. The Co-doped TiO_2 sample showed an absorption edge at 424 nm, which is redshifted relative to the bare TiO_2. The UV–visible DRS analysis illustrated that bare and Co-doped TiO_2 have bandgaps of 2.75 and 2.6 eV, respectively (Supplementary Fig. S1b). The observed redshift in the absorption spectra can be ascribed to $Co^{2+} \rightarrow Ti^{4+}$ charge-transfer[53]. Thus, photoluminescence (PL) emission spectroscopy was utilized to study the fate of the photoinduced charge carriers[54]. Oxygen vacancies and surface states play a vital role in the photocatalytic response of anatase TiO_2[55]. Supplementary Fig. S1c shows the room-temperature PL spectra of the bare and Co-doped TiO_2 samples, where eight peaks started from 396 nm and ended at 700 nm were recorded[56]. The detected superimposed multi-peaks
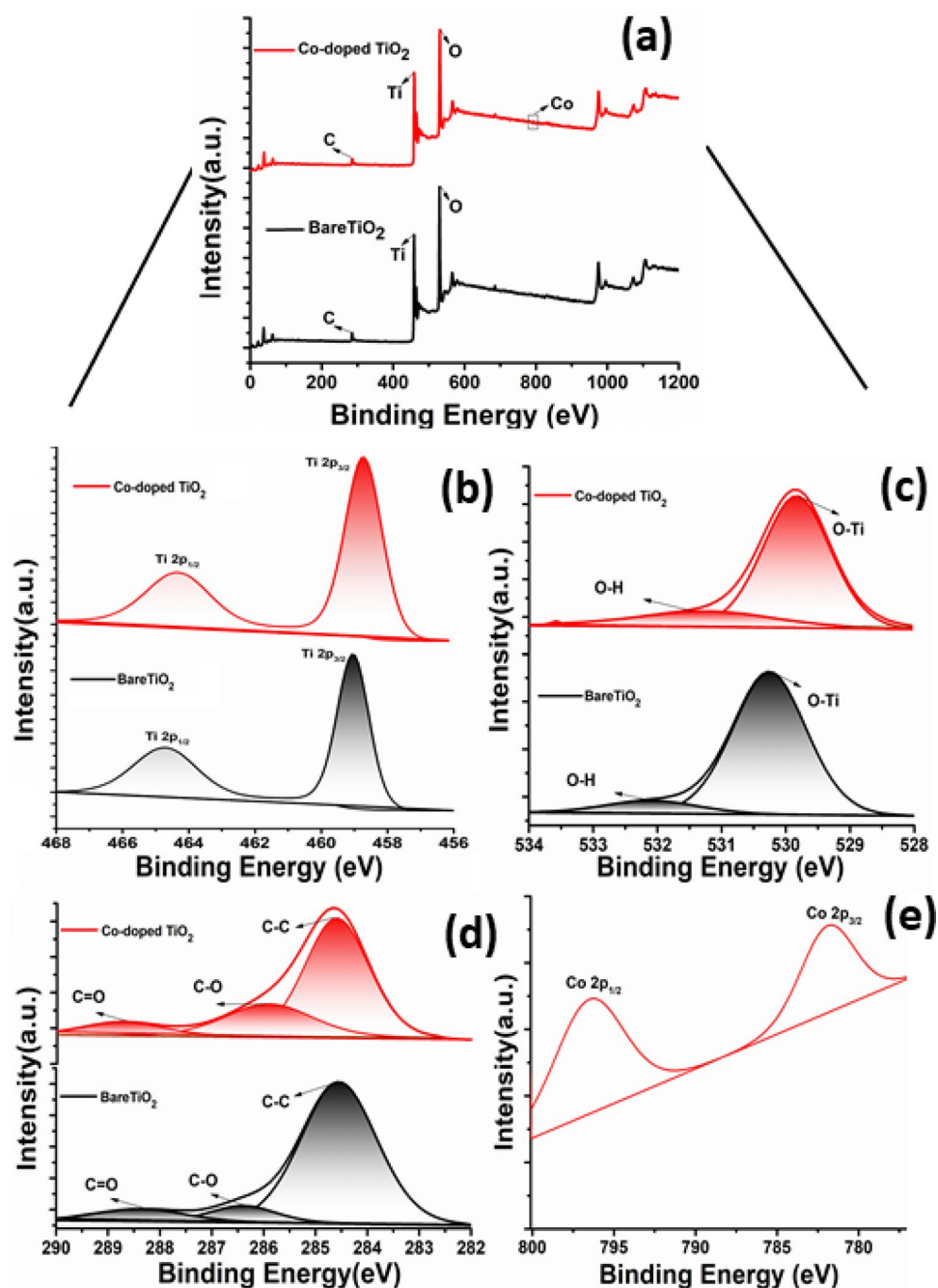
Figure 2. XPS spectra of bare and Co-doped TiO_2 mesocrystals: (**a**) survey spectra, and the HR-spectra of (**b**) Ti 2p, (**c**) O 1 s, (**d**) C 1 s, and (**e**) Co 2p.

may reveal radiative recombination of electron–hole pairs from different energy levels[57]. Notably, the Co-doped TiO_2 exhibited a decrease in the PL peaks intensity compared to the bare TiO_2, indicating a reduction in the recombination rate of charge carriers in the Co-doped TiO_2 sample[58]. These results suggest the superior photocatalytic activity of Co-doped TiO_2 mesocrystals over bare TiO_2 mesocrystals.

Antimicrobial properties. Usually antimicrobial agents are used to hinder microbial diseases emanating from clinical poisoning, such as urinary tract infection (UTI)-causing microbes[31]. However, nanomaterials-based agents have recently received great attention as they are uniquely-applied to combat pathogenic microbes[59]. In our study, the fabricated samples were checked for their antimicrobial capabilities using the disc agar diffusion technique. The TiO_2 samples were found to deactivate a broad spectrum of the tested bacteria such as *P. aeruginosa*, *P. mirabilis*, and *S. aureus*. Specifically, Co-doped TiO_2 mesocrsytals showed the most powerful antibacterial effect against all examined microbes, see Fig. 4, Supplementary Fig. S2 and Supplementary Table S1. The
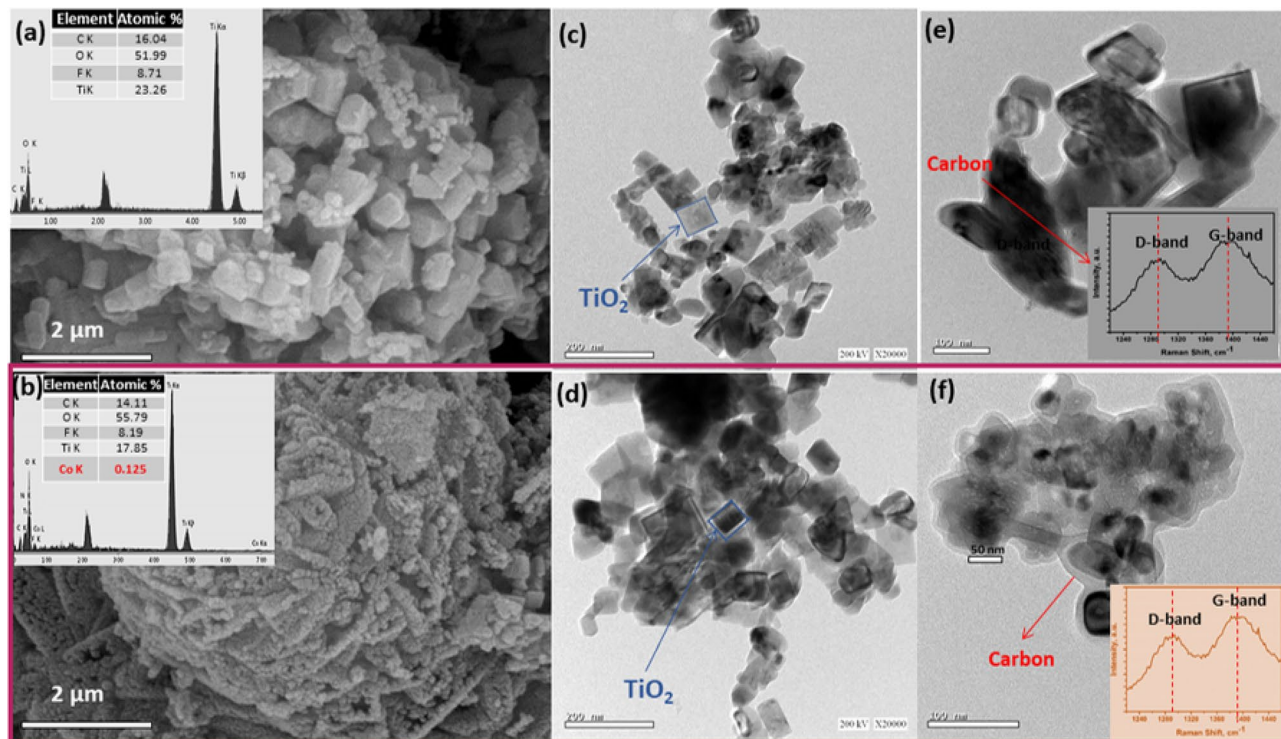
Figure 3. (**a**,**b**) FESEM images, (**a**,**b** insets) EDX analysis, (**c**–**f**) HR-TEM images and (**e**,**f** insets) Raman spectra of bare and Co-doped TiO_2 mesocrystals.
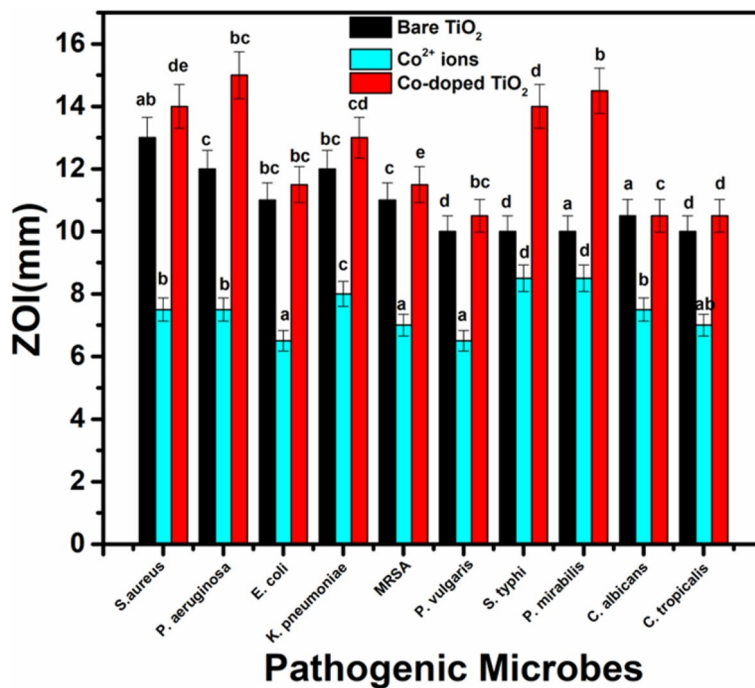

Figure 4. Antimicrobial activity of bare TiO_2 NPs and Co-doped TiO_2 NPs against different pathogenic microbes as ZIO. The data within the groups are analyzed using a one-way analysis of variance (ANOVA) followed by[a,b,c,d,e] Duncan's multiple range test.
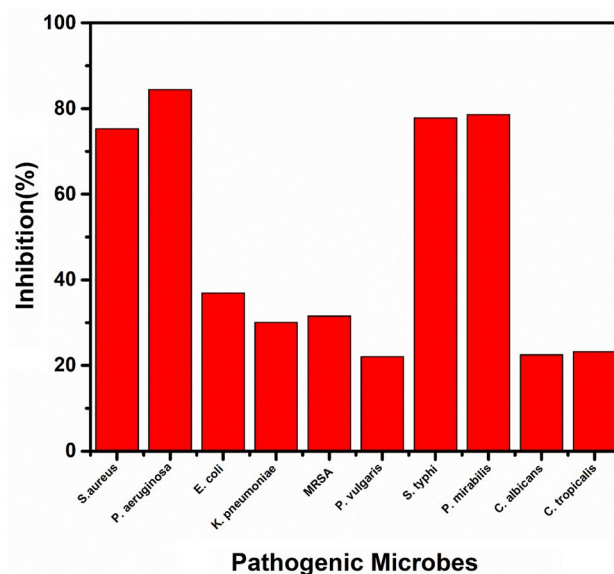
Figure 5. Antibiofilm activity of Co-doped TiO$_2$ against different pathogenic microbes as inhibition %.

antimicrobial abilities of the samples were compared with Co^{2+} ions and standard antibacterial and antifungal agents like Amoxicillin (AX; 25 μg/mL) and Nystatin (NS; 25 μg/mL). Our samples are found to be more active than the used standard antibiotics, and Co^{2+} ions. Interestingly, the synthesized TiO$_2$ mesocrystals were found to be more active against Gram-negative bacteria than the Gram-positive counterpart because the cell wall of the Gram-negative bacteria contains a thick layer of lipopolysaccharide essentially in addition to a small layer of peptidoglycan. On contrary, Gram-positive bacteria primarily incorporate a thicker layer of peptidoglycan blocks[29]. The fabricated NPs enjoy high surface-to-volume ratio, thus can be easily combined and interact with some of the pathogenic microbes, such as yeasts, bacteria, and fungi yeast[30].

The MIC results ranged from 0.39 to 25 μg/mL of the integrated samples against all tested microbes. The promising MIC of the Co-doped TiO$_2$ mesocrystals was 0.39 μg/mL (*P. aeruginosa*), and 0.781 μg/mL (*P. mirabilis*). Additionally, the synthesized Co-doped TiO$_2$ NPs exhibit accepted MIC of 12.5 μg/mL against *C. albicans* at very low NPs concentration (10.0 μg/mL), suggesting their potential use as antifungal agents. Importantly, the properties of the synthesized mesocrystals play a vital role in their antimicrobial characteristics, including their structure, purity, and size[51–54]. Various advanced mechanisms, such as reactive oxygen species (ROS) distribution (superoxide anion; O$_2^-$), were proposed in the literature to explain the possible effects of a plethora of metal oxides as antibacterial agents[60–63]. However, the antimicrobial mechanism of Co-doped TiO$_2$ mesocrystals has not been identified yet. Thus, the interaction of Co-doped TiO$_2$ mesocrystals with the pathogenic microbes and the alkaline tendency have been included here to demonstrate the possible antimicrobial activity mechanism. It is suggested that Co-doped TiO$_2$ mesocrystals could alter the microbial morphology and their film composition, change the microbial membrane permeability, and produce the residence of oxidative stress genes via the production of H$_2$O$_2$[60]. Note that Co^{2+} ions were shown to possess antibacterial activity, where a series of Co^{2+} complexes of mercapto-thiadiazole-derived furanyl, thienyl, pyrrolyl, salicylic, and pyridinyl Schiff bases exhibited in-vitro weak to moderate antibacterial potential toward Gram-negative bacteria (*Escherichia coli*, *Pseudomonas aeruginosa*, *Salmonella typhi*, and *Shigella flexneri*) and Gram-positive bacteria (*Bacillus subtilis* and *Staphylococcus aureus*)[64]. Another study by Gaëlle et al.[65] showed that the ligands, metal salt, and the complexes (Cobalt (II) complex [Co(phen)$_3$(NO$_3$)$_2$]·2H$_2$ O and a novel Co (III) complex) were investigated for their antimicrobial potentials in-vitro toward pathogenic bacteria and fungi. The antimicrobial results indicated that all ligands were very effective towards the tested microbes. The antibacterial activity of pure cobalt or Co^{2+} ions was attributed to the reaction with negatively-charged molecules inside the microbial cells, which in turn leads to genotoxicity and destruction of the main bacterial organelles[31].

Antibiofilm activity of Co-doped TiO$_2$ mesocrystals. The formation of biofilm in pathogenic microbes is characterized by the exo-polysaccharide secretion[28,29]. The tube method was applied to determine the antibiofilm potential of the synthesized Co-doped TiO$_2$ mesocrystals against some UTI-producing microbes. Supplementary Fig. S3 shows the antibiofilm action of the Co-doped TiO$_2$ mesocrystals for *Pseudomonas aeruginosa* and *Candida albicans*. The complete steps are: (I) Normal microbial growth and production of the distinct ring in the lack of the synthesized Co-doped TiO$_2$ mesocrystals and the interference with microbial growth in the closeness of Co-doped TiO$_2$ mesocrystals, (II) The probability of staining of the formed biofilm with Crystal Violet (CV), which is a qualitative determination method, and (III) Eliminating and separating the adhered microbial cells after ethanol addition for semi-quantitative estimation of the biofilm hindrance % (Supplementary Table S2). Supplementary Fig. S3a shows the tube design for the determination of antibiofilm potential of Co-doped TiO$_2$ against *P. aeruginosa*, the sensitive bacteria example, which creates a thick whitish-yellow layer
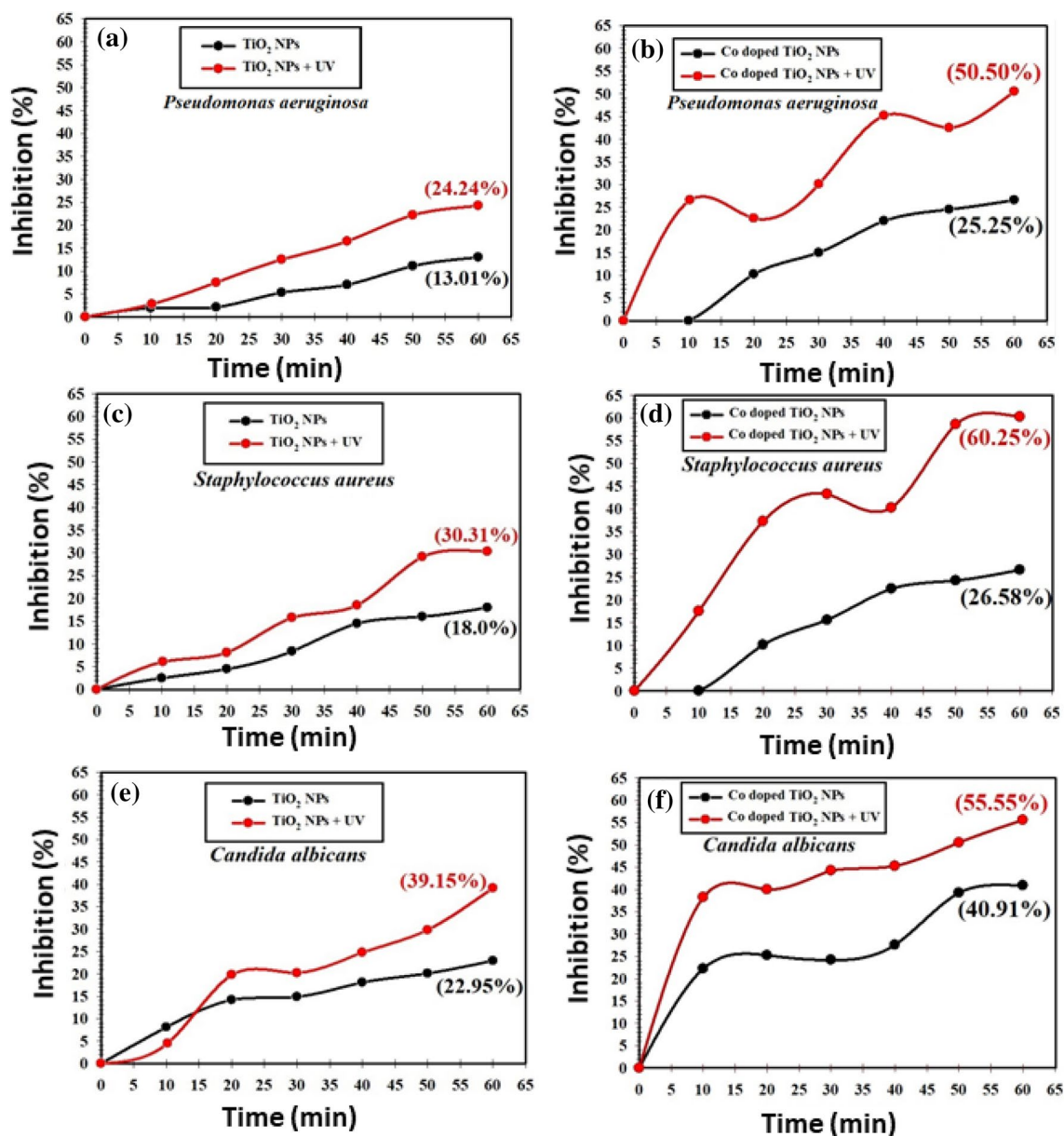
Figure 6. Antimicrobial effect under UV-irradiation effect against different pathogenic microbes, where *Pseudomonas aeruginosa* (**a,b**), *Staphylococcus aureus* (**c,d**), and *Candi1da albicans* (**e,f**), using of bare TiO$_2$, and Co-doped TiO$_2$ in liquid media, respectively.

in the air–liquid interface in the lake of the mesocrystals (control). The produced matt layers were fully-adhered across the walls of the designed tubes and developed as a blue color following the staining with CV. Next, a dark blue color was created in the produced solution subsequent dissolving CV with absolute ethanol, as presented in Supplementary Fig. S3a. On the other side, in the tubes including *P. aeruginosa* cells and in the closeness of Co-doped TiO$_2$ mesocrystals (10 µg/mL), a remarkable negative effect was recognized as the cells of the tested bacteria do not form biofilm layers and the ring formation was blocked. Also, the adherent cell color was quiet and the blue color was faintly-formed after ethanol addition, as displayed in Supplementary Fig. S3a. Related forms were shown for the biofilm repression of the tested yeast *C. albicans* as presented in Supplementary Fig. S3b. The semi-quantitative determination of the inhibition percentage (%) was investigated by a UV–visible spectrophotometer. The optical density (O.D.) was estimated at 570 nm following terminating CV-stained biofilms, which were considered as a means of their creation. Supplementary Table S2 displays the inhibition% following the addition of 10.0 µg/mL Co-doped TiO$_2$ mesocrystals, revealing that the highest percentage for *P. aeruginosa* is 84.43%, for *P. mirabilis* is 78.58%, and for *S. typhi* is 77.81%. Note that Co-doped TiO$_2$ mesocrystals were able to control the biofilm growth at its adhesion degree, which is the first step in the antimicrobial process[66]. The change in the inhibition percentage may be ascribed to many factors such as the high potential of the antimicrobial agents to be attached to the surface due to the high surface area of the synthesized Co-doped TiO$_2$ mesocrystals and their particle size as well as the invasion skills and different chemical characteristics influencing the relationship and communication of Co-doped TiO$_2$ mesocrystals with biofilms-producing microbes[67]. Positively, the synthesized
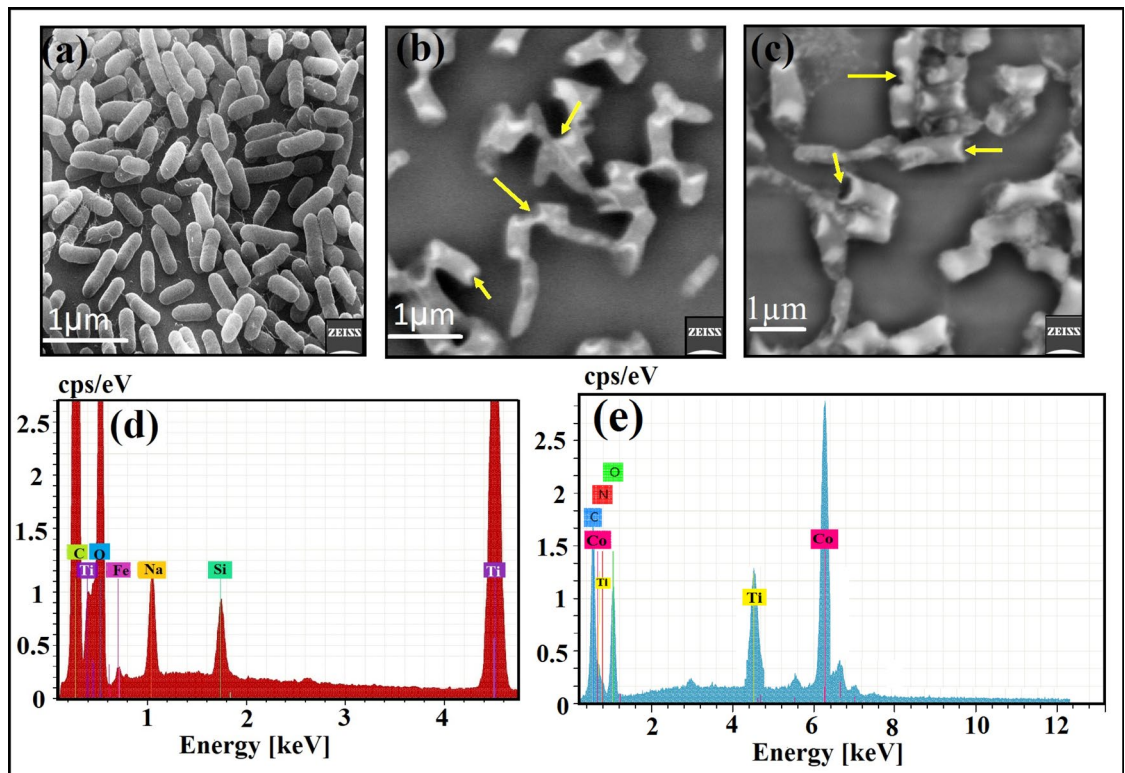
Figure 7. SEM and the matching EDX elemental study of *P. aeuroginosa*: (**a**) Regular bacterial cells (*P. aeuroginosa*) without TiO₂ mesocrystals, and Co-doped TiO₂ mesocrystals treatment, (**b**) Abnormal, deformed and irregular bacterial cell with incomplete lysis following TiO₂ mesocrystals treatment, (**c**) Fully-irregular and deformed bacterial cell through Co-doped TiO₂ mesocrystals treatment presenting the full lysis of *P. aeuroginosa* cell, (**d**) Matching EDX elemental study of the treated *P. aeuroginosa* cell validating the cellular internalization of the qualified TiO₂ mesocrystals in *P. aeuroginosa* cells, and (**e**) Matching EDX elemental examination of the treated *P. aeuroginosa* cell establishing the cellular internalization of the integrated Co-doped TiO₂ mesocrystals in *P. aeuroginosa* cells.

Co-doped TiO₂ mesocrystals suppressed the growth of *P. aeruginosa* by more than 98% with 0.39 μg/mL MIC as listed in Supplementary Table S2. Figure 5 shows a summarized diagram regarding the antibiofilm potential of Co-doped TiO₂ mesocrystals (as inhibition %) against different pathogenic microbes.

Antimicrobial effect of Co-doped TiO₂ in liquid media under illumination.

The comparison between the inhibition% of *P. aeruginosa*, *S. aureus*, and *C. albicans* upon the use of TiO₂ and Co-doped TiO₂ mesocrystals and UV are presented in Fig. 6. Note that Co-doped TiO₂ showed higher antimicrobial activities against *P. aeruginosa, S. aureus,* and *C. albicans* colonies than pure TiO₂, Fig. 6b–d, revealing the synergistic actions of Co doping and the TiO₂ mesocrystals. Moreover, upon UV-illumination, Co-doped TiO₂ mesocrystals exhibited even higher antimicrobial activities than that in the dark. The maximum inhibition percentage of bare TiO₂ and Co-doped TiO₂ mesocrystals under UV-illumination for *P. aeruginosa* at the end of the experiment was 24.24% and 50.50%, respectively (Fig. 6a,b), while it was 30.31% and 60.25% for *S. aureus* (Fig. 6c,d), and 39.15% and 55.55% for *C. albicans* (Fig. 6e,f).

The observed activity under light irradiation may be related to the induced oxygen species such as OH free radicals, which caused the destruction of the microbial coenzymes and reduced their contents[19,42]. The major influences involve the creation of holes in the cell wall of the microbes, which subsequently-progressed the cell permeability and finally a cell death will occur. To confirm the induced oxygen species, electron paramagnetic resonance (EPR) spectra were collected as shown in Supplementary Fig. S4. The two samples showed signals at $g = 1.95$, $g = 2.157$, $g = 2.05$, and $g = 2.12$, confirming the presence of Ti³⁺ and free oxygen radicals such as OH·, O·⁻, or O_2^{-}[68]. Notably, the Co-doped TiO₂ sample showed a higher concentration of paramagnetic centers of 4.16953×10^{18} spin/g relative to the bare TiO₂ sample (4.09473×10^{18} spin/g). The increased paramagnetic centers after the addition of cobalt may be related to the increase in the concentration of oxygen radicals in the TiO₆ lattice[57]. This is in agreement with the inhabitation % of Co-doped versus bare TiO₂.

SEM/EDX analysis was performed to elucidate the possible antimicrobial mechanism toward *P. aeuroginosa*, see Fig. 7. The SEM analysis of the control sample in the absence of any mesocrystals showed bacterial groups that are constantly-developed with typical normal bacterial surface and semi-formed biofilm, Fig. 7a. Upon TiO₂ mesocrystals treatment, noticeable morphological differences were identified in *P. aeuroginosa* (Fig. 7b), including the incomplete lysis of the outer surface followed by deformations of the *P. aeuroginosa* cells. Additionally, Co-doped
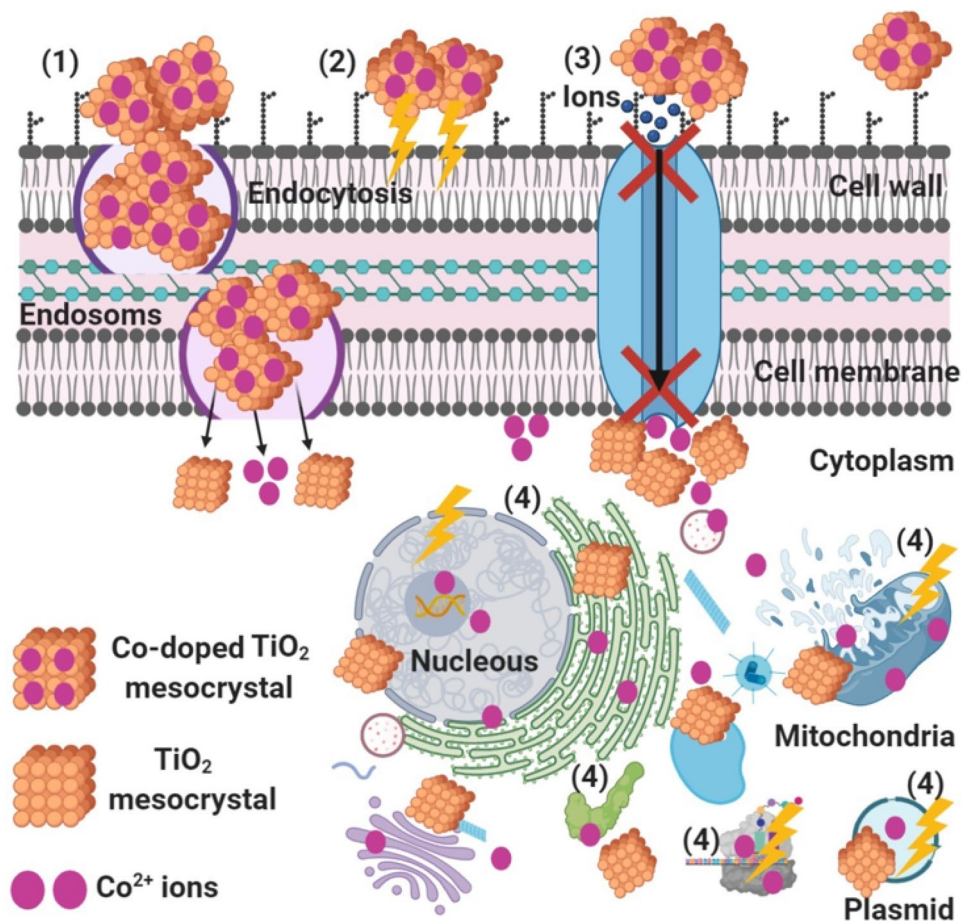
Figure 8. Schematic representation regarding the four prominent ways of antimicrobial potential of Co-doped TiO₂ mesocrystals, where (1) Co-doped TiO₂ mesocrystals adhere to the bacterial cell surface and results in membrane damage and altered transport activity; (2) Co-doped TiO₂ mesocrystals create and increase the ROS leading to cell damage, (3) Co-doped TiO₂ mesocrystals block the ions transport from and to the bacterial cell, and (4) Co-doped TiO₂ mesocrystals penetrate inside the bacterial cells and interact with cellular organelles and biomolecules, and thereby, affect respective cellular machinery, and modulate the cellular signal system and causing cell death. Co-doped TiO₂ mesocrystals may serve as a vehicle to effectively-deliver Co ions to the bacterial cytoplasm and membrane, where proton motive force would decrease the pH to be less than 3.0 and therefore improve the release of Co ions.

TiO₂ mesocrystals caused the entire and complete lysis of the bacterial cell with the decrease in the whole viable number, and ultimately the biofilm growth was restrained (Fig. 7c). The EDX elemental analysis shows the presence of Ti and O elements with others from the bacteria like C, and O, along with Fe, Si, and Na form the microelement in the bacterial medium. All detected elements were located at the malformed cities and the outside surface of the *P. aeuroginosa* cells, validating the performance of the tested TiO₂ mesocrystals, (Fig. 7d). Finally, the EDX elemental spectra, in case of Co-doped TiO₂, revealed Co, Ti, and O elements along with different atoms from the bacterial structure at the irregular areas and at the outside surface of the treated *P. aeuroginosa* cells.

The schematic in Fig. 8 illustrates the possible antibacterial mechanism. We believe that Co-doped TiO₂ mesocrystals start their action by adhesion at the outer surface of the bacterial cell, causing membrane damage and altered transport activity. Then, diffusion of Co^{2+} inside the bacterial cell (at pH = 3) and dividing all of the intracellular structure like mitochondria, plasmid, DNA, and other vital organelles. Afterwards, cellular toxicity occurs due to the oxidative stress generated by the production of ROS. Finally, TiO₂ mesocrystals were withstood the acidic condition inside the bacterial cells and conversion did not occur[69] but possessed the antibacterial effect by affecting the signal transduction pathways.

Conclusion

In summary, unique multi-doped TiO₂ mesocrystals have been synthesized via a facile sol–gel approach. The crystal structure, optical, and compositional properties of the materials were elucidated using XRD, Raman, FTIR, XPS UV–vis analyses. The synthesized Co-doped TiO₂ mesocrystals showed excellent antimicrobial activity compared to bare TiO₂ counterparts. The antimicrobial performance was evaluated in terms of zone of inhibition, minimum inhibitory concentration (MIC), antibiofilm activity, and photoactivity. Co-doped TiO₂ mesocrystals

showed 60.25% inactivation of *S. aureus* after 60 min of UV illumination. The SEM findings supported the results of the viability tests, demonstrating complete lysis of the bacterial cells with the decrease in the whole viable number. The Co-doped TiO_2 mesocrystals showed very promising MIC of 0.390 μg/mL and 0.781 μg/mL for *P. mirabilis* and *P. mirabilis*, respectively. Additionally, the material showed an MIC of 12.5 μg/mL against *C. albicans*, suggesting its use as antifungal agent. Considering the efficient fast and oxidative damage mediated inactivation of bacteria on the Co-doped TiO_2 mesocrystals showed in this study, our results supports further development and application of Co-doped TiO_2 mesocrystals in other fields.

References

1. Navya, P. N. & Daima, H. K. Rational engineering of physicochemical properties of nanomaterials for biomedical applications with nanotoxicological perspectives. *Nano Converg.* **3**, 1–14 (2016).
2. Abbas, W., Ali, B. A., Abdullah, I. M., Ahmed, N. & Allam, N. K. Recent advances in the use of TiO_2 nanotubes powder in biological, environmental, and energy applications. *Nanoscale Adv.* **1**, 2801–2816 (2019).
3. Cölfen, H. & Antonietti, M. Mesocrystals: Inorganic superstructures made by highly parallel crystallization and controlled alignment. *Angew. Chemie Int. Ed.* **44**, 5576–5591 (2005).
4. Sturm, E. V. & Cölfen, H. Mesocrystals: Structural and morphogenetic aspects. *Chem. Soc. Rev.* **45**, 5821–5833 (2016).
5. Yao, X. *et al.* Simultaneous photocatalytic degradation of ibuprofen and H_2 evolution over Au/sheaf-like TiO_2 mesocrystals. *Chemosphere* **261**, 127759 (2020).
6. Samir, M., Ahmed, N., Ramadan, M. & Allam, N. K. Electrospun mesoporous Mn-V-O@C nanofibers for high performance asymmetric supercapacitor devices with high stability. *ACS Sustain. Chem. Eng.* **7**, 13471–13480 (2019).
7. Chen, Y.-F., Tang, X.-N., Zhang, B., Luo, Y. & Li, Y. TiO_2@SiO_2 composites: Preparation and photocatalytic antimicrobial performance. *J. Inorg. Mater.* **34**, 1325–1333 (2019).
8. Hegazy, A. H. *et al.* TiO_2 nanoparticles optimized for photoanodes tested in large area dye-sensitized solar cells (DSSC). *Sol. Energy Mater. Sol. Cells* **153**, 108–116 (2016).
9. Ahmed, N., Ramadan, M., Farghali, A. A., El Rouby, W. M. A. & Allam, N. K. Non-precious co-catalysts boost the performance of TiO_2 hierarchical hollow mesoporous spheres in solar fuel cells. *Int. J. Hydrogen Energy* **43**, 21219–21230 (2018).
10. Ismael, A. M. *et al.* Novel TiO_2/GO/$CuFe_2O_4$ nanocomposite: A magnetic, reusable and visible-light-driven photocatalyst for efficient photocatalytic removal of chlorinated pesticides from wastewater. *RSC Adv.* **10**, 34806–34814 (2020).
11. Hayden, S. C., Allam, N. K. & El-Sayed, M. A. TiO_2 nanotubes/CdS hybrid electrodes:Extraordinarily enhancement in the inactivation of *Escherichia coli. J. Am. Chem. Soc.* **132**, 14406–14408 (2010).
12. Vatansever, F. *et al.* Antimicrobial strategies centered around reactive oxygen species—bactericidal antibiotics, photodynamic therapy, and beyond. *FEMS Microbiol. Rev.* **37**, 955–989 (2013).
13. Xia, P. *et al.* Designing a 0D/2D S-scheme heterojunction over polymeric carbon nitride for visible-light photocatalytic inactivation of bacteria. *Angew. Chem. Int. Ed.* **59**, 5218–5225 (2020).
14. Abdelhafiz, A. A. *et al.* Defect engineering in 1D Ti-W oxide nanotube arrays and their correlated photoelectrochemical performance. *Phys. Chem. Chem. Phys.* **20**, 10258–10265 (2018).
15. Ibrahim, E. M., Hasan, M. M., Saleh, A. A. & Allam, N. K. Structural engineering of Ti–Mn bimetallic phosphide nanotubes for efficient photoelectrochemical water splitting. *Int. J. Hydrogen Energy* **46**, 3605–3614 (2021).
16. Deyab, N. M., Salem, K. E., Mokhtar, A. M., Ramadan, M. & Allam, N. K. Electrochemical fabrication of ternary black Ti–Mo–Ni oxide nanotube arrays for enhanced photoelectrochemical water oxidation. *ChemistrySelect* **5**, 12151–12158 (2020).
17. El-Shazly, A. N., Hegazy, A. H., Rashad, M. M., El-Shahat, M. F. & Allam, N. K. Ultrathin ALD TiO_2 shells for enhanced photoelectrochemical solar fuel generation. *J. Alloys Compd.* **739**, 178–183 (2018).
18. El-shazly, A. N., Hegazy, A. H., El Shenawy, E. T., Hamza, M. A. & Allam, K. Solar energy materials and solar cells novel facet-engineered multi-doped TiO_2 mesocrystals with unprecedented visible light photocatalytic hydrogen production. *Sol. Energy Mater. Sol. Cells* **220**, 110825 (2021).
19. Fawzy, S. M., Omar, M. A. & Allam, N. K. Photoelectrochemical water splitting by defects in nanostructured multinary transition metal oxides. *Sol. Energy Mater. Sol. Cells* **194**, 184–194 (2019).
20. Soliman, M. M. *et al.* On the relationship between rutile/anatase ratio and the nature of defect states in sub-100 nm TiO_2 nanostructures: Experimental insights. *Phys. Chem. Chem. Phys.* **20**, 5975–5982 (2018).
21. Li, X., Guo, Z. & He, T. The doping mechanism of Cr into TiO_2 and its influence on the photocatalytic performance. *Phys. Chem. Chem. Phys.* **15**, 20037–20045 (2013).
22. Gao, B. *et al.* Synthesis of yellow mesoporous Ni-doped TiO_2 with enhanced photoelectrochemical performance under visible light. *Inorg. Chem. Front.* **4**, 898–906 (2017).
23. Zhao, X. G. & Huang, L. Q. Iridium, carbon and nitrogen multiple-doped TiO_2 nanoparticles with enhanced photocatalytic activity. *Ceram. Int.* **43**, 3975–3980 (2017).
24. Charanpahari, A., Umare, S. S. & Sasikala, R. Effect of Ce, N and S multi-doping on the photocatalytic activity of TiO_2. *Appl. Surf. Sci.* **282**, 408–414 (2013).
25. Wang, R. *et al.* Graphdiyne-modified TiO_2 nanofibers with enhanced photocatalytic antibacterial and osteoinductive activities for implant infection. *Nat. Commun.* **11**, 4465 (2020).
26. Hegazy, A. & Prouzet, E. Room temperature synthesis and thermal evolution of porous nanocrystalline TiO_2 anatase. *Chem. Mater.* **24**, 245–254 (2012).
27. Christensen, G. D., Simpson, W. A., Bisno, A. L. & Beachey, E. H. Adherence of slime-producing strains of *Staphylococcus epidermidis* to smooth surfaces. *Infect. Immun.* **37**, 318–326 (1982).
28. Ansari, M. A., Khan, H. M., Khan, A. A., Cameotra, S. S. & Pal, R. Antibiofilm efficacy of silver nanoparticles against biofilm of extended spectrum β-lactamase isolates of *Escherichia coli* and *Klebsiella pneumoniae*. *Appl. Nanosci.* **4**, 859–868 (2014).
29. Maksoud, M. I. A. *et al.* Antibacterial, antibiofilm, and photocatalytic activities of metals-substituted spinel cobalt ferrite nanoparticles. *Microb. Pathog.* **127**, 144–158 (2019).
30. El-Batal, A. I., El-Sayyad, G. S., Al-Hazmi, N. E. & Gobara, M. Antibiofilm and antimicrobial activities of silver boron nanoparticles synthesized by PVP polymer and gamma rays against urinary tract pathogens. *J. Clust. Sci.* **30**, 947–964 (2019).
31. Abd Elkodous, M. *et al.* Therapeutic and diagnostic potential of nanomaterials for enhanced biomedical applications. *Colloids Surfaces B Biointerfaces* **180**, 411–428 (2019).
32. El-Nemr, K. F., Mohamed, H. R., Ali, M. A., Fathy, R. M. & Dhmees, A. S. Polyvinyl alcohol/gelatin irradiated blends filled by lignin as green filler for antimicrobial packaging materials. *Int. J. Environ. Anal. Chem.* https://doi.org/10.1080/03067319.2019.1657108 (2019).

33. Chen, W. F. *et al.* Effects of precipitation, liquid formation, and intervalence charge transfer on the properties and photocatalytic performance of cobalt- or vanadium-doped TiO_2 thin films. *Int. J. Hydrogen Energy* https://doi.org/10.1016/j.ijhydene.2016.08.115 (2016).
34. Niu, H. *et al.* Visible-light active and magnetically recyclable nanocomposites for the degradation of organic dye. *Materials (Basel).* **7**, 4034–4044 (2014).
35. Lontio Fomekong, R. & Saruhan, B. Synthesis of Co^{3+} doped TiO_2 by co-precipitation route and its gas sensing properties. *Front. Mater.* **6**, 1–6 (2019).
36. Ohsaka, T. Temperature dependence of the Raman spectrum in anatase TiO_2. *J. Phys. Soc. Jpn.* **48**, 1661–1668 (1980).
37. Samir, M., Salama, M. & Allam, N. K. Sub-100 nm TiO_2 tubular architectures for efficient solar energy conversion. *J. Mater. Chem. A* **4**, 9375–93805 (2016).
38. Saleh, A. A., Farag, M. & Allam, N. K. Correlation between microstructural defects and photoelectrochemical performance of one-dimensional Ti-Nb composite oxide photoanodes for solar water splitting. *Int. J. Hydrogen Energy* **44**, 24418–24429 (2019).
39. Shao, X., Lu, W., Zhang, R. & Pan, F. Enhanced photocatalytic activity of TiO_2-C hybrid aerogels for methylene blue degradation. *Sci. Rep.* **3**, 1–9 (2013).
40. Faid, A. F. & Allam, N. K. Stable solar-driven water splitting by anodic ZnO nanotubular semiconducting photoanodes. *RSC Adv.* **6**, 80221–80225 (2016).
41. Samsudin, E. M., Abd Hamid, S. B., Juan, J. C., Basirun, W. J. & Centi, G. Synergetic effects in novel hydrogenated F-doped TiO_2 photocatalysts. *Appl. Surf. Sci.* **370**, 380–393 (2016).
42. El-Sayed, A. *et al.* Defect states determined the performance of dopant-free anatase nanocrystals in solar fuel cells. *Sol. Energy* **144**, 445–452 (2017).
43. Zhang, Y. *et al.* The influence of reaction temperature on the formation and photocatalytic hydrogen generation of (001) faceted TiO_2 nanosheets. *ChemNanoMat* **1**, 270–275 (2015).
44. Kumaravel, V. *et al.* Indium-doped TiO_2 photocatalysts with high-temperature anatase stability. *J. Phys. Chem. C* **123**, 21083–21096 (2019).
45. Akshay, V. R. *et al.* Observation of optical band-gap narrowing and enhanced magnetic moment in co-doped sol-gel-derived anatase TiO_2 nanocrystals. *J. Phys. Chem. C* **122**, 26592–26604 (2018).
46. Liu, G. *et al.* Synthesis, characterization and photocatalytic evaluation of visible light activated C-doped TiO_2 nanoparticles. *Nanotechnology* **23**, 294003 (2012).
47. Liu, C. *et al.* Controlled charge-dynamics in cobalt-doped TiO_2 nanowire photoanodes for enhanced photoelectrochemical water splitting. *J. Colloid Interface Sci.* **530**, 403–411 (2018).
48. Siddiqa, A., Masih, D., Anjum, D. & Siddiq, M. Cobalt and sulfur co-doped nano-size TiO_2 for photodegradation of various dyes and phenol. *J. Environ. Sci.* **37**, 100–109 (2015).
49. Hasan, M., Tolba, S. & Allam, N. K. In-situ formation of graphene stabilizes the zero-valent copper nanoparticles and significantly enhances the efficiency of photocatalytic water splitting. *ACS Sustain. Chem. Eng.* **6**, 16876–16885 (2018).
50. Vasei, M., Das, P., Cherfouth, H., Marsan, B. & Claverie, J. P. TiO_2@C core-shell nanoparticles formed by polymeric nano-encapsulation. *Front. Chem.* **2**, 1–9 (2014).
51. Schito, A. & Corrado, S. An automatic approach for characterization of the thermal maturity of dispersed organic matter Raman spectra at low diagenetic stages. *Geol. Soc. London, Spec. Publ.* **484**, 107–119 (2018).
52. Mai, W., Wen, F., Xie, D., Leng, Y. & Mu, Z. Structure and composition study of carbon-doped titanium oxide film combined with first principles. *J. Adv. Ceram.* **3**, 49–55 (2014).
53. Khan, M. A., Al-Oufi, M., Tossef, A., Al-Salik, Y. & Idriss, H. On the role of CoO in CoO_x/TiO_2 for the photocatalytic hydrogen production from water in the presence of glycerol. *Catal. Struct. React.* **1**, 192–200 (2015).
54. Yu, J. G. *et al.* The effect of calcination temperature on the surface microstructure and photocatalytic activity of TiO_2 thin films prepared by liquid phase deposition. *J. Phys. Chem. B* **107**, 13871–13879 (2003).
55. Khan, H. & Swati, I. K. Fe^{3+}-doped anatase TiO_2 with d-d transition, oxygen vacancies and Ti^{3+} centers: Synthesis, characterization, UV-vis photocatalytic and mechanistic studies. *Ind. Eng. Chem. Res.* **55**, 6619–6633 (2016).
56. Pan, S. *et al.* Engineering the intermediate band states in amorphous Ti^{3+}-doped TiO_2 for hybrid dye-sensitized solar cell applications. *J. Mater. Chem. A* **3**, 11437–11443 (2015).
57. Su, C. H., Hu, C. C., Sun, Y. C. C. & Hsiao, Y. C. Highly active and thermo-stable anatase TiO_2 photocatalysts synthesized by a microwave-assisted hydrothermal method. *J. Taiwan Inst. Chem. Eng.* **59**, 229–236 (2016).
58. Hashem, E. M. *et al.* Novel Z-scheme/type-II $CdS@ZnO/g-C_3N_4$ ternary nanocomposites for the durable photodegradation of organics: Kinetic and mechanistic insights. *Chemosphere* https://doi.org/10.1016/j.chemosphere.2020.128730 (2020).
59. Karthik, K., Dhanuskodi, S., Gobinath, C., Prabukumar, S. & Sivaramakrishnan, S. Fabrication of MgO nanostructures and its efficient photocatalytic, antibacterial and anticancer performance. *J. Photochem. Photobiol. B Biol.* **190**, 8–20 (2019).
60. El-Batal, A. I., Al-Hazmi, N. E., Mosallam, F. M. & El-Sayyad, G. S. Biogenic synthesis of copper nanoparticles by natural polysaccharides and *Pleurotus ostreatus* fermented fenugreek using gamma rays with antioxidant and antimicrobial potential towards some wound pathogens. *Microb. Pathog.* **118**, 159–169 (2018).
61. Mosallam, F. M., El-Sayyad, G. S., Fathy, R. M. & El-Batal, A. I. Biomolecules-mediated synthesis of selenium nanoparticles using *Aspergillus oryzae* fermented Lupin extract and gamma radiation for hindering the growth of some multidrug-resistant bacteria and pathogenic fungi. *Microb. Pathog.* **122**, 108–116 (2018).
62. Tang, Z. X. & Lv, B. F. MgO nanoparticles as antibacterial agent: Preparation and activity. *Braz. J. Chem. Eng.* **31**, 591–601 (2014).
63. Karthik, K., Shashank, M., Revathi, V. & Tatarchuk, T. Facile microwave-assisted green synthesis of NiO nanoparticles from *Andrographis paniculata* leaf extract and evaluation of their photocatalytic and anticancer activities. *Mol. Cryst. Liq. Cryst.* **673**, 70–80 (2018).
64. Chohan, Z. H., Pervez, H., Rauf, A., Khan, K. M. & Supuran, C. T. Antibacterial cobalt (II), copper (II), nickel (II) and zinc (II) complexes of mercaptothiadiazole—Derived furanyl, thienyl, pyrrolyl, salicylyl and pyridinyl Schiff bases. *J. Enzyme Inhib. Med. Chem.* **21**, 193–201 (2006).
65. Gaëlle, D. S. Y., Yufanyi, D. M., Jagan, R., Agwara, M. O. & Bradshaw, D. Synthesis, characterization and antimicrobial properties of cobalt(II) and cobalt(III) complexes derived from 1,10-phenanthroline with nitrate and azide co-ligands. *Cogent Chem.* **2**, 1253201 (2016).
66. Ashajyothi, C., Harish, K. H., Dubey, N. & Chandrakanth, R. K. Antibiofilm activity of biogenic copper and zinc oxide nanoparticles-antimicrobials collegiate against multiple drug resistant bacteria: A nanoscale approach. *J. Nanostruct. Chem.* **6**, 329–341 (2016).
67. Park, H. J. *et al.* Removal characteristics of engineered nanoparticles by activated sludge. *Chemosphere* **92**, 524–528 (2013).
68. Wang, X., Yan, Y., Hao, B. & Chen, G. Biomimetic layer-by-layer deposition assisted synthesis of Cu, N co-doped TiO_2 nanosheets with enhanced visible light photocatalytic performance. *Dalt. Trans.* **43**, 14054–14060 (2014).
69. Liu, W., Sun, W., Borthwick, A. G. L. & Ni, J. Comparison on aggregation and sedimentation of titanium dioxide, titanate nanotubes and titanate nanotubes-TiO_2: Influence of pH, ionic strength and natural organic matter. *Colloids Surfaces A Physicochem. Eng. Asp.* **434**, 319–328 (2013).

Acknowledgements

Author contributions

A.N.E., A.H.H., and M.A.H. synthesized and characterized the mesocrystals, and analyzed the results. G.S.E. and R.M.F. performed the antimicrobial experiments and analyzed the results. N.K.A. analyzed the results and coordinated the project. All authors contributed to the writing of the manuscript.

Competing interests

The authors declare no competing interests.

Additional information

Supplementary Information The online version contains supplementary material available at https://doi.org/10.1038/s41598-021-84989-x.

Correspondence and requests for materials should be addressed to N.K.A.

Reprints and permissions information is available at www.nature.com/reprints.

Publisher's note Springer Nature remains neutral with regard to jurisdictional claims in published maps and institutional affiliations.